

# Soft-phonon anharmonicity, floppy modes, and Na diffusion in $\text{Na}_3\text{FY}$ ( $Y = \text{S, Se, Te}$ ): *Ab initio* and machine-learned molecular dynamics simulations

Mayanak Kumar Gupta,<sup>\*</sup> Sajan Kumar, Ranjan Mittal<sup>†</sup> and Samrath L. Chaplot<sup>‡</sup>

*Solid State Physics Division, Bhabha Atomic Research Centre, Mumbai, 400085, India  
and Homi Bhabha National Institute, Anushaktinagar, Mumbai 400094, India*



(Received 22 April 2022; revised 1 July 2022; accepted 11 July 2022; published 25 July 2022)

A class of Na-based antiperovskites  $\text{Na}_3\text{XY}$  ( $X = \text{F, H; } Y = \text{S, Se, Te}$ ) was recently reported with a remarkably high ionic conductivity  $\sim 0.1$  mS/cm near room temperature. Herein, we report comprehensive atomic dynamics investigations using *ab initio* and large-scale machine-learned molecular dynamics (MLMD) simulation on these sodium superionic conductors. Previous studies identified the role of soft phonons involving rotations of  $\text{FNa}_6$  octahedral units in Na diffusion. In contrast, our MLMD simulations show that the Na diffusion pathways are essentially uncorrelated and do not involve the collective dynamics of octahedral rotations or reorientations. Moreover, while the soft phonons do not involve any  $Y$  atomic dynamics, the diffusion pathways are sterically hindered unless facilitated by  $Y$  displacements and Na vacancies. However, we do find that the anharmonic low-energy phonon modes of wave vectors along the  $M$ - $R$  line at the Brillouin zone (BZ) boundary are important precursors of Na diffusion. These modes involve vibrations perpendicular to the F-Na ionic bond, along  $\langle 100 \rangle$  directions, which provide the initial pathways for the Na diffusion. We have calculated the branch-resolved phonon spectral energy density (SED) in the entire BZ using the MLMD simulations. The SED results as a function of temperature reveal the large anharmonicity of the soft phonon modes, which leads to floppy dynamics of Na atoms. The volume of cubic- $\text{Na}_3\text{FS}$  is the smallest among the three antiperovskites and has the largest mean-phonon energy. Our calculated Na diffusion coefficient at 700 K in  $\text{Na}_3\text{FS}$  of  $\sim 0.63 \times 10^{-6}$  cm<sup>2</sup>/s is significantly larger than  $\sim 0.16 \times 10^{-6}$  cm<sup>2</sup>/s in  $\text{Na}_3\text{FTe}$ , which clearly shows contrast with the hypothesis of a softer lattice leading to faster diffusion. The estimated diffusion barrier energy for  $\text{Na}_3\text{FS}$  with 2% Na vacancy is  $\sim 0.44$  eV, which is in fair agreement with the reported value of 0.44 eV estimated from the total conductivity measurement with Na-vacant iodine-doped  $\text{Na}_3\text{FS}$ . Similarly, for  $\text{Na}_3\text{FSe}$  and  $\text{Na}_3\text{FTe}$ , the barrier energies have been estimated to be 0.50 and 0.55 eV, respectively. Our large-scale MLMD-based theoretical study provides a comprehensive understanding of the role of soft phonons, host dynamics, and vacancies in Na diffusion in  $\text{Na}_3\text{FY}$  ( $Y = \text{S, Se, Te}$ ) and other materials of this class, which will be helpful in designing materials for application in solid-state batteries.

DOI: [10.1103/PhysRevB.106.014311](https://doi.org/10.1103/PhysRevB.106.014311)

## I. INTRODUCTION

The recent global thrust in the electrification of vehicles and the search for renewable energy resources demand more materials for energy applications [1–6]. Hence, to meet the future energy demand, a widespread effort seeks to accelerate the design and discovery of materials with more abundant elements such as Na. This requires a detailed understanding of the influence of the material structure and dynamics on ionic transport properties. Na-based solid state ionic conductors such as NASICON have shown great potential as candidates for solid state electrolytes [7–12]. However, their high processing cost and relatively high temperature needed to achieve significant Na conductivity have so far limited their usability in practical applications. Still, significant research efforts are ongoing to address these issues. A few Na-based

compounds, such as Na-thiophosphate, Na-thioantimonate, and their derivatives, have recently been discovered to show good ionic conductivity at room temperature [13–18]. Detailed investigations based on neutron scattering, impedance spectroscopy, and molecular dynamics (MD) simulations of these materials suggest that ionic conductivity in these materials is strongly governed by anharmonic low-energy host modes and the presence of Na vacancies [19–29]. The  $PnY_4$  ( $Pn = \text{P, Sb; } Y = \text{S, Se}$ ) tetrahedral units in these materials form the framework structure, and Na ions are arranged in channels running through the framework structure [12,19–23,25–29]. It is important to note that the rotational dynamics of these tetrahedral framework units are known to accelerate Na hopping [12,14,19,21–23,25–29]. In our previous studies on Li/Na-based materials, we identified the importance of reorientation dynamics and phonon anharmonicity of the host for fast Li/Na diffusion [13,30–33].

Perovskites are simple compounds consisting of octahedral units whose rotational and tilt distortions lead to rich phase diagrams and tunable electronic, optic, and thermal

<sup>\*</sup>mayankg@barc.gov.in

<sup>†</sup>rmittal@barc.gov.in

properties, including superconductivity, negative thermal expansion, and multiferroicity. Many perovskites are known to have the potential for energy storage applications [34–38]. In recent years, Li- and Na-rich antiperovskites (*electronically inverted* perovskites) have become promising candidate materials for solid state batteries based on their high ionic conductivity, wide electrochemical window, stability, and low cost [34]. In the past few years, many antiperovskites have been discovered to show superionic conductivity [37–41]. Alkali-rich antiperovskite compounds  $M_3BA$  ( $A$  and  $B$  = anions,  $M$  = the metal cation), such as lithium-rich antiperovskites (LiRAPs) [38,42–44] and sodium-rich antiperovskites (NaRAPs) [35–37,45], have shown significant Li/Na conductivity and have the potential to become a class of viable solid electrolytes. The compounds  $\text{Li}_3\text{OCl}$  and  $\text{Li}_3\text{OCl}_{0.5}\text{Br}_{0.5}$  exhibit very high Li conductivities. Similarly, Na-based antiperovskites such as  $\text{Na}_3\text{OX}$  ( $X = \text{Cl}, \text{Br}, \text{I}, \text{BH}_4, \text{NO}_2$ ), also exhibit high Na ion conductivity [36,37,46]. Recently, the potassium-rich antiperovskite  $\text{K}_{2.9}\text{Ba}_{0.05}\text{OI}$  also has been explored by Zheng *et al.* [47]; it shows excellent ionic conductivity, although at relatively high temperatures ( $\sigma \sim 3.5 \times 10^{-3}$  S/cm at 523 K). Authors of a number of works tuned the vacancy concentration via doping, changing the stoichiometric ratio, and replacing cation and anion with suitable elements to enhance ion conductivity and energy barriers [45,48–50]. Notably, all antiperovskites tend to have some Li/Na vacancies, which are critical to the onset diffusion. In addition, these compounds also show strongly anharmonic phonon behaviors [35,51], usually characteristics of perovskites [52–54]. It is therefore essential to understand the relative influence of vacancies and phonon anharmonicity on Na/Li conductivity to identify the critical descriptors in the search and design of antiperovskites for solid-electrolyte applications.

Recently, a class of Na antiperovskites,  $M_3XY$  ( $X = \text{F}, \text{H}; Y = \text{S}, \text{Se}, \text{Te}$ ), has been discovered [35], showing promising conductivity. A detailed investigation based on Raman, impedance spectroscopy measurements, and harmonic lattice dynamics simulation on hydride antiperovskites ( $M_3\text{HY}$ ) and fluoride antiperovskites ( $M_3\text{FY}$ ) showed that the electronegativity of the B-site element (H vs F) does not significantly impact Li/Na conductivity [55]. However, the selection of more polarizable A-site chalcogens reduces the Na/Li conductivity [35]. Surprisingly, this contrasts with other superionic materials containing S and Se (e.g.,  $\text{Na}_3\text{PS}_4$  and  $\text{Na}_3\text{PSe}_4$ ), where a more polarizable host-lattice exhibits higher ionic conductivity ( $\sigma_{\text{Na}_3\text{PS}_4} > \sigma_{\text{Na}_3\text{PSe}_4}$ ) [17,56,57]. What is also surprising is that the Na migration barrier is largest in  $\text{Na}_3\text{FTe}$ , which has the largest unit cell volume and hence is expected to have wider migration pathways, while the smaller unit cell  $\text{Na}_3\text{FS}$  exhibits the smallest barrier among the three [35]. The authors also proposed that the low-energy (low- $E$ ; here,  $E$  is phonon mode energy) anharmonic modes along  $M$ - $R$  directions in the cubic Brillouin zone (BZ), which correspond to rotation and tilt of  $\text{YM}_6$  octahedra, facilitate the Na conductivity [35]. The authors also performed the total conductivity measurements in cubic iodine-doped  $\text{Na}_3\text{HSe}$  ( $\sim 1 \times 10^{-4}$  S/cm at 375 K) [35] and iodine-doped  $\text{Li}_3\text{FSe}$  ( $\sim 2 \times 10^{-4}$  S/cm at 375 K) [35] and estimated activation energy for Li/Na hopping  $\sim 0.44$  eV.

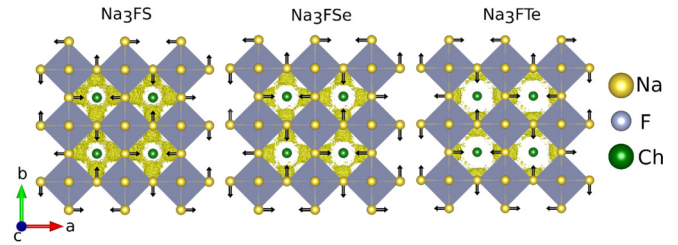


FIG. 1. The crystal structure of  $\text{Na}_3\text{FY}$  ( $Y = \text{S}, \text{Se}, \text{Te}$ ) in the cubic phase. Here, Na, F, and Y (S, Se, and Te) atoms are shown by yellow, light blue, and green colors, respectively. We have shown one of the representative low- $E$  phonon modes at the  $M$  point ( $\frac{1}{2}, \frac{1}{2}, 0$ ), which involves the displacement of Na, while F and Ch are at rest. Such low- $E$  modes are precursors of Na hopping in antiperovskites. The machine-learned molecular dynamics (MLMD) calculated Na-probability density isosurface plot (shown by small yellow dots) of cubic- $\text{Na}_3\text{FY}$  ( $Y = \text{S}, \text{Se}, \text{Te}$ ) with 2% Na vacancies at 700 K. The cubic lattice parameters used in our calculations on  $\text{Na}_3\text{FY}$  ( $Y = \text{S}, \text{Se}, \text{Te}$ ) are 4.437, 4.509, and 4.703 Å for  $Y = \text{S}, \text{Se},$  and  $\text{Te}$ , respectively. We have used a  $(4 \times 4 \times 4)$  supercell trajectory up to 500 ps projected on a single unit cell to compute the Na probability distribution.

In this paper, we present a detailed investigation of anharmonic lattice dynamics and Na diffusion in the recently discovered Na-based antiperovskites,  $M_3\text{FY}$  ( $Y = \text{S}, \text{Se}, \text{Te}$ ). The compound  $\text{Na}_3\text{FS}$  crystallizes in an orthorhombic phase (space group =  $Pbnm$ ) at room temperature, while  $\text{Na}_3\text{FSe}$  and  $\text{Na}_3\text{FTe}$  are cubic (space group  $Pm\bar{3}m$ ; Fig. 1) [35]. Using *ab initio* MD (AIMD) and state-of-the-art machine-learned MD (MLMD) simulations, we have investigated the respective roles of Na vacancies and low-energy phonon modes across the BZ. We discuss how the difference in anharmonicity of the low-energy phonon modes in  $M_3\text{FY}$  ( $Y = \text{S}, \text{Se}, \text{Te}$ ) influences the Na diffusion and its magnitude. We investigate the importance of Na vacancies to onset Na conductivity and their influence on phonon dynamics. Further, large-scale MLMD simulations allow us to probe the minimum energy hopping pathways and their associated barrier energies.

## II. COMPUTATIONAL DETAILS

### A. Lattice dynamics

*Ab initio* lattice dynamics calculations were performed within the density functional theory framework implemented in the Vienna *Ab initio* Simulation Package (VASP) [58,59]. The calculations were done using the projector-augmented wave formalism [60] and used the generalized gradient approximation exchange-correlation functional parameterization by Perdew, Burke, and Ernzerhof [61,62]. The phonon calculations were performed on a  $3 \times 3 \times 3$  supercell using the finite displacement method implemented in PHONOPY software [63]. A  $4 \times 4 \times 4$  k-point mesh was generated using the Monkhorst-Pack method [64], and a plane-wave energy cutoff of 600 eV was used. The convergence criteria for electronic and ionic minimizations were set to  $10^{-8}$  eV and  $10^{-3}$  eV Å $^{-1}$ , respectively.

## B. MD

AIMD simulations were performed with the same  $3 \times 3 \times 3$  supercell and an energy cutoff of 600 eV. However, we used a coarser electronic convergence criteria ( $10^{-6}$  eV) and a single k-point at the zone center during the AIMD simulation. AIMD simulations were performed from 100 to 1000 K in intervals of 100 K within the NVT framework, and the temperatures were controlled using a Nosé-Hoover thermostat [64] with a time constant of 0.1 ps. All the simulations were run for 10–15 ps with a time step of 2 fs.

We have used the DEEPM code [65] based on a deep neural network algorithm to generate a neural network force-field that reproduces as best as possible the AIMD results. Subsequent MLMD simulations were performed with this machine-learned potential using LAMMPS [66]. We used the dp utility for training, testing, and generation of the forcefield. The AIMD dataset (energies and forces from 100 to 900 K with an interval of 100 K) was used for training the neural network forcefield. A cutoff of 8.0 Å for neighbor atom interaction and the embedding and fitting network sizes are set to (25, 50, 100) and (240, 240, 240), respectively. The generated forcefield was used to compute various thermodynamical quantities [pair distribution function (PDF), phonon density of states (PDOS), and mean squared displacement (MSD)] and checked against AIMD results. We have also compared AIMD vs MLMD computed forces and energies. We found an excellent agreement between the MLMD vs AIMD results.

Many earlier works have used the MLMD method to simulate solids and liquids [6,13,67–70]. In our recent work on Na and Cu-based superionic materials, we have successfully utilized this method to understand and analyze the neutron scattering experiments [6,13]. In Na<sub>3</sub>FY ( $Y = \text{S, Se, Te}$ ), we have extensively tested the potential by computing various thermodynamical properties, energies, and forces using AIMD vs MLMD in Fig. S1 in the Supplemental Material [71], which confirms the robustness of the method.

We performed the MLMD simulations within an NVT ensemble on a  $4 \times 4 \times 4$  supercell of the cubic-Na<sub>3</sub>FY structure with both stoichiometric composition and with 2% Na vacancies. We computed the trajectories up to 600 ps with 1 fs time steps. The phonon spectral energy density (SED) was performed based on MLMD on a  $20 \times 20 \times 20$  supercell of cubic-Na<sub>3</sub>FY up to 100 ps, which provides  $Q$  and  $E$  resolutions of 0.05 rlu and 1 meV, respectively. Further, the influence of the host lattice dynamics was investigated by performing a constrained MD simulation by freezing the chalcogenides and F elements.

The PDOS  $g(E)$  was computed from the Fourier transform of the velocity autocorrelation function [ $C(t)$ ], as defined below:

$$g(E) = \int C(t) \exp\left(\frac{iEt}{\hbar}\right) dt, \quad (1)$$

$$C(t) = \sum_{i=1}^N \frac{\langle \vec{v}_i(0) \vec{v}_i(t) \rangle}{\langle \vec{v}_i(0) \vec{v}_i(0) \rangle}, \quad (2)$$

where  $\vec{v}_i(t)$  is the velocity of the  $i$ th element at any instant time  $t$ , and the symbol of the ensemble average is denoted by  $\langle \dots \rangle$ .

The MSD of the  $i$ th element ( $\langle u_i^2(t) \rangle$ ) at time  $t$  was calculated using

$$\langle u_i^2(t) \rangle = \frac{1}{N_i} \sum_{k=1}^{N_i} \langle |\vec{r}_i^k(t) - \vec{r}_i^k(0)|^2 \rangle, \quad (3)$$

where  $N_i$  is the total number of the  $i$ th species in the simulation cell, and  $\vec{r}_i^k(t)$  is the position of the  $k$ th particle of the  $i$ th type element at time  $t$ .

The diffusion constant of the  $i$ th species at a given temperature  $D(T)$  was estimated using the Einstein relation:

$$D(T) = \lim_{t \rightarrow \infty} \frac{\langle u_i^2(t) \rangle}{6t}. \quad (4)$$

The time-averaged pair-distribution function  $g_{ij}(r)$  between the  $i$ th and  $j$ th elements was calculated using [72]

$$g_{ij}(r) = \frac{V}{4\pi r^2 N} \sum_{i \neq j} \langle \delta(r - |\vec{r}_i - \vec{r}_j|) \rangle, \quad (5)$$

where  $N$  is the number of atoms,  $\vec{r}_i$  is the position coordinates,  $\delta(\dots)$  is the Dirac delta function, and  $\langle \dots \rangle$  indicates the time average over the total simulation time.

The presence of correlations and nature of Na diffusion (i.e., jumplike vs continuous diffusion) were investigated by computing the distinct and self-Van Hove correlation functions  $G_d^{ij}(r, t)$  and  $G_s^i(r, t)$  defined as [73,74]

$$G_d^{ij}(r, t) = \frac{1}{N} \left\langle \sum_{i \neq j} \delta(r - |\vec{r}_i(t) - \vec{r}_j(0)|) \right\rangle, \quad (6)$$

$$G_s^i(r, t) = \frac{1}{N} \left\langle \sum_{i=1}^N \delta(r - |\vec{r}_i(t) - \vec{r}_i(0)|) \right\rangle. \quad (7)$$

Here,  $N$  is the number of particles, and  $\vec{r}_i(t)$  is the position of the  $i$ th atom at time  $t$ .

To study the temperature-dependent phonon properties, the SED [ $\varphi(\vec{q}, E)$ ] has been calculated in a  $20 \times 20 \times 20$  supercell containing  $\sim 40\,000$  atoms for cubic-Na<sub>3</sub>FY using MLMD trajectories using the following relation. The SED at the wave vector  $\vec{q}$  and energy  $E$  is defined as [75]

$$\begin{aligned} \varphi(\vec{q}, E) = & \frac{1}{4\pi \tau_0 N} \sum_{\alpha, k} m_k \\ & \times \left| \sum_{n=1}^N \int_0^{\tau_0} \vec{u}_\alpha \left( \begin{matrix} n \\ k \end{matrix}; t \right) \exp \left[ i\vec{q}\vec{r} \left( \begin{matrix} n \\ k \end{matrix} \right) - \frac{iEt}{\hbar} \right] dt \right|^2, \end{aligned} \quad (8)$$

where  $N$  is the number of unit cells in a supercell ( $N = N_1 \times N_2 \times N_3$ ), the summation index  $\alpha$  runs over Cartesian  $x$ ,  $y$ , and  $z$ ; the index  $k$  runs over the number of particles in the unit cell,  $m_k$ ,  $\vec{r}_k^n$  are the mass of the  $k$ th atom and its equilibrium position in the  $n$ th unit cell, and  $\vec{u}_\alpha \left( \begin{matrix} n \\ k \end{matrix}; t \right)$  is the velocity of the  $k$ th atom in the  $n$ th unit cell at time  $t$ . An MD simulation with a supercell dimension ( $N_1 \times N_2 \times N_3$ ) and trajectory length of  $\tau_0$  ps gives an energy resolution of  $\Delta E = 4.136/\tau_0$  meV and the smallest wave vectors of  $\Delta \vec{q} = \frac{2\pi}{aN_1} \hat{i}$ ,  $\frac{2\pi}{aN_2} \hat{j}$ , and  $\frac{2\pi}{aN_3} \hat{k}$ , respectively. Here,  $a$  is the lattice parameter of the cubic cell.

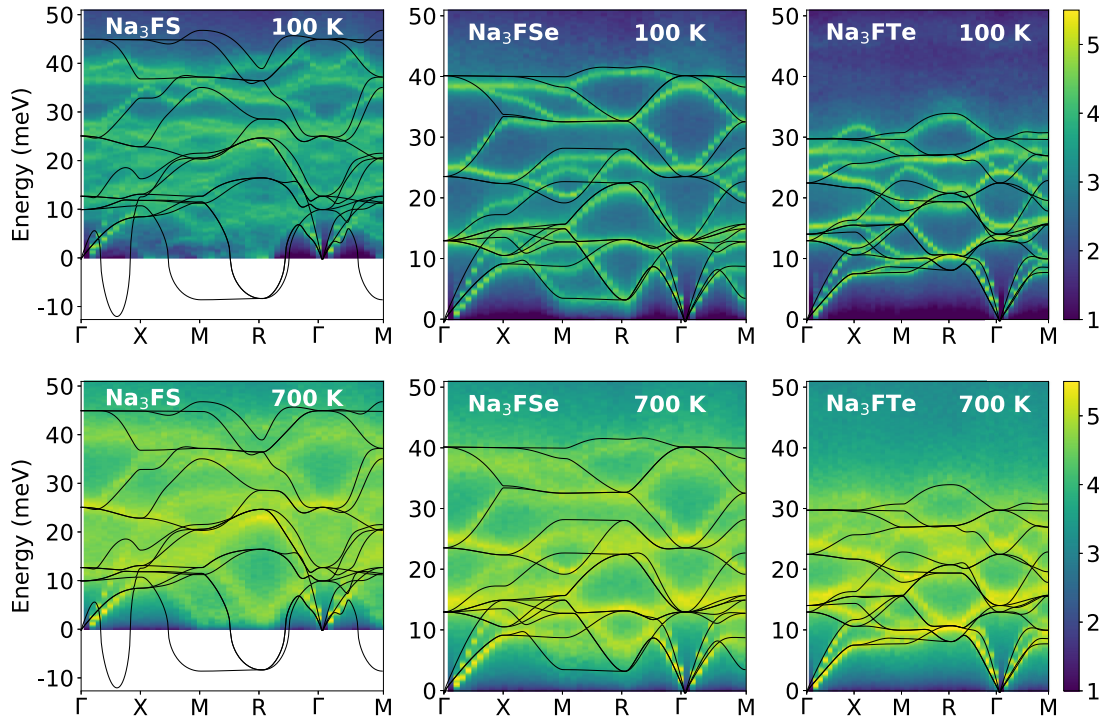


FIG. 2. The calculated phonon dispersion relation (solid black line) in cubic  $\text{Na}_3\text{FY}$  ( $Y = \text{S}, \text{Se}, \text{Te}$ ) using *ab initio* lattice dynamics at  $T = 0 \text{ K}$ . The machine-learned molecular dynamics (MLMD) calculated spectral energy density at 100 and 700 K, in the upper and lower panels, respectively. Low- $E$  modes get stabilized at 700 K and show large linewidth, which is the signature of strong phonon anharmonicity. More interestingly,  $\text{Na}_3\text{FS}$  shows a significant shift in the energy of low- $E$  phonon modes, followed by  $\text{Na}_3\text{FSe}$ , while  $\text{Na}_3\text{FTe}$  low- $E$  modes do not show much change with temperature.

### III. RESULT AND DISCUSSIONS

#### A. Harmonic phonons dynamics

In the harmonic picture of lattice vibrations, a Taylor expansion of the free energy surface is truncated at the second order (harmonic), which results in well-defined phonon quasiparticles, and hence, they are represented by delta functions (zero width). However, all the materials show finite linewidths of phonon spectra attributed to higher-order anharmonic terms of the potential energy surface. A dominant contribution of higher-order terms in the potential energy surface would lead to renormalized phonon frequencies and significant broadening in the spectral lines, which significantly affect the thermodynamical and transport properties of materials. Usually, superionic conductors exhibit a large thermal vibrational amplitude and a shallow potential surface and tend to exhibit a strong anharmonic effect. We discuss the effect of strong anharmonicity on phonons of  $\text{Na}_3\text{FY}$  ( $Y = \text{S}, \text{Se}, \text{Te}$ ) in the next section.

To survey the overall phonons and nature of dynamics in the cubic phase of  $\text{Na}_3\text{FY}$  ( $Y = \text{S}, \text{Se}, \text{Te}$ ), we have performed harmonic *ab initio* lattice dynamics calculations at 0 K. The calculated phonon dispersion relations are shown in Fig. 2. The calculated dispersion in cubic  $\text{Na}_3\text{FS}$  shows unstable modes, indicating that a lower-symmetry structure exists at 0 K, consistent with the experimental observation of the orthorhombic phase at low temperature [35] (Fig. 2). The presence of unstable modes is a descriptor of strong anharmonicity in atomic dynamics of respective modes at

high temperatures. Phonon renormalization by anharmonicity stabilizes these unstable modes at elevated temperatures, leading to a dynamically stable cubic- $\text{Na}_3\text{FS}$  phase. In contrast,  $\text{Na}_3\text{FSe}$  and  $\text{Na}_3\text{FTe}$  show stable phonon dispersions over the entire BZ, even at the quasiharmonic level. In the next section, we investigate the SED at high temperatures to reveal the influence of mode anharmonicity in stabilizing the phonon modes and their evolution with temperature.

The low- $E$  phonon modes are observed across the  $M$ - $R$  line in the BZ in all three compounds. In Fig. 1, we show the eigenvector of one of the representative low- $E$  modes at the  $M$  point ( $\frac{1}{2} \frac{1}{2} 0$ ) phonon mode. These modes lead to a large vibrational amplitude of Na atoms perpendicular to the F-Na bond along the  $\langle 100 \rangle$  directions, which help Na ions to reach the saddle point along the minimum energy pathways and lead to diffusion. In Fig. S2 in the Supplemental Material [71], we plot the species-resolved partial PDOS at 0 K, which shows that significant Na dynamics occur at low  $E$ .

Further, we show in Fig. S2 in the Supplemental Material [71] that the overall phonon spectral range and mean phonon frequency of all the elements in  $\text{Na}_3\text{FY}$  shift to lower energy for heavier/larger chalcogens  $\text{S} \rightarrow \text{Se} \rightarrow \text{Te}$ . Also, the overlap between the  $Y$  and Na PDOS decreases from S to Se to Te. Surprisingly, the phonon band center vs Na conductivity shows a negative correlation, unlike in other Li/Na-based superionics, which show a positive correlation [22,57]. This indicates that the average phonon behavior is an insufficient quantity to provide a good descriptor for Na conductivity.

### B. Anharmonic atomic dynamics and Na hopping

To further investigate the Na diffusion process, we have performed MLMD simulations at different temperatures with and without Na vacancies. The temperature dependence of the calculated PDOS of cubic  $\text{Na}_3\text{FY}$  ( $Y = \text{S}, \text{Se}, \text{Te}$ ) with vacancies shows significant broadening of the PDOS upon increasing temperature (Fig. S3 in the Supplemental Material [71]). We note that the degree of broadening of the phonon peaks is higher in  $\text{Na}_3\text{FS}$  than in the other two compositions  $\text{Na}_3\text{FY}$  ( $Y = \text{Se}, \text{Te}$ ). However, it is challenging to isolate the phonon energy shift and associated anharmonicity of specific modes from the PDOS alone; thus, we now focus on the phonon SED calculation.

To probe the mode and direction-resolved phonon anharmonicity, we have computed the phonon SED at 100 and 700 K. Results are shown in Fig. 2. For comparison, we overplot the harmonic phonon dispersions as solid black lines. At 100 K, the SED in  $\text{Na}_3\text{FS}$  overlaps well with the harmonic phonon dispersions for acoustic modes and some high-energy optical modes. However, it already shows significant deviations from the harmonic calculation for a number of branches across the BZ. This shift between the harmonic calculation and the positions of SED peaks is a direct manifestation of anharmonic dynamics in  $\text{Na}_3\text{FS}$  even at 100 K. Further, the SED shows finite intensity at  $E \sim 0$  meV along the  $M$ - $R$  segment and prominent intensity at  $M$  and  $R$  points. This infers the strong damping of low-lying phonon modes, which appear as imaginary modes in the harmonic calculation. The large intensity at  $M$  and  $R$  points indicates that these are precursor fluctuations that become Bragg points in the low- $T$  orthorhombic phase. At 700 K, these low- $E$  modes along the  $M$ - $R$  line in the BZ are anharmonically stabilized to  $\sim 2$  meV. We emphasize that these modes are very broad, with their width comparable with the mode energy, indicating that they are strongly damped oscillations and have very large vibrational amplitudes.

In comparison with  $\text{Na}_3\text{FS}$ , the SED in  $\text{Na}_3\text{FSe}$  and  $\text{Na}_3\text{FTe}$  show relatively sharp phonon peaks at 100 K that match well with the 0 K harmonic phonon dispersions. The low- $E$  modes along the  $M$ - $R$  line are sharper and stiffer than that in  $\text{Na}_3\text{FS}$ . At 700 K, the low- $E$  mode across the  $M$ - $R$  line hardens significantly in  $\text{Na}_3\text{FSe}$ , while  $\text{Na}_3\text{FTe}$  does not show any visible change. Overall, we find a significant broadening and hardening of low- $E$  modes across the  $M$ - $R$  line on warming in all three compounds, but  $\text{Na}_3\text{FS}$

shows the largest change. This trend establishes that the low- $E$  modes in  $\text{Na}_3\text{FS}$  are particularly strongly anharmonic and overdamped, more so than in  $\text{Na}_3\text{FSe}$  and  $\text{Na}_3\text{FTe}$ .

We observe a nearly flat soft phonon dispersion along the  $M(\frac{1}{2}\frac{1}{2}0)$ - $R(\frac{1}{2}\frac{1}{2}\frac{1}{2})$  line in the BZ. In fact, considering all the symmetry-equivalent wave vectors, these soft modes occur over all 12 edges of the cubic BZ. This infers a simultaneous population of these strongly anharmonic low- $E$  modes over a large range of wave vectors. In combination, because of their large anharmonic amplitudes and wave vectors spanning entire BZ edges, these rotational modes appear as uncorrelated Na vibrations, which may be termed as the floppy modes [54,76]. The Na vibrational amplitudes due to the soft phonons would be large in the direction perpendicular to the F-Na ionic bond, that is, along the  $\langle 100 \rangle$  directions. At high temperatures, these floppy modes act as precursors for Na diffusion. This is revealed by observing the Na trajectories discussed below. We have also calculated the SED with 2% Na vacancies (Fig. S4 in the Supplemental Material [71]), which does not show any significant change in the phonon dynamics behavior between the stoichiometric and off-stoichiometric (vacancy) structure up to 2% of Na vacancy concentration.

We also observe that the energy of low-lying modes along  $M$ - $R$  follows an increasing trend from S to Se to Te, which infers a larger vibrational amplitude in  $\text{Na}_3\text{FS}$  than the other two compounds. However, the broadening (i.e., anharmonicity) of these low-lying modes along  $M$ - $R$  follows a decreasing trend from S to Se to Te. This trend is also consistent with the magnitude of the diffusion constant in the three compounds, suggesting that anharmonicity plays an important role in this class of compounds.

### C. Na diffusion, migration pathways, and correlations

From the MLMD simulations on stoichiometric cubic  $\text{Na}_3\text{FY}$  ( $Y = \text{S}, \text{Se}, \text{Te}$ ), we calculated the MSD at  $T = 100, 300,$  and  $700$  K. Results are shown in Fig. S5 in the Supplemental Material [71]. In the stoichiometric compositions, we do not find any evidence of Na diffusion even up to 1 ns simulation times, consistent with prior investigations of Na-based superionic materials [13,14,18,21]. The effect of Na vacancies on Na diffusivity was investigated by performing MLMD simulations with 2% Na vacancies in cubic  $\text{Na}_3\text{FY}$  ( $Y = \text{S}, \text{Se}, \text{Te}$ ) at 100, 300, and 700 K (Fig. S3 in the Supplemental

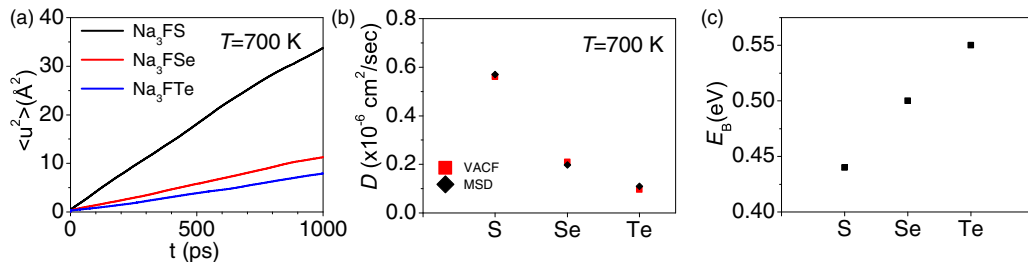


FIG. 3. (a) The machine-learned molecular dynamics (MLMD) calculated Na-mean squared displacement (MSD) in cubic  $\text{Na}_3\text{FY}$  ( $Y = \text{S}, \text{Se}, \text{Te}$ ) with 2% Na vacancies at 700 K. The  $\text{Na}_3\text{FS}$  shows the largest Na-MSD, while  $\text{Na}_3\text{FTe}$  has the least Na-MSD. (b) The estimated Na diffusion constant from Na-MSD and integrating the velocity autocorrelation function (VACF) of Na, respectively. (c) The activation energy barrier for Na migration estimated from Na probability density calculation [77].

TABLE I. The calculated barrier energy using Na probability isosurface density in cubic- $\text{Na}_3\text{FY}$  ( $Y = \text{S, Se, Te}$ ) with 2% Na vacancies at 700 K.

	$\rho_{\text{th}}$ (threshold density) ( $\text{\AA}^{-3}$ )	$\rho_{\text{max}}$ (maximum density) ( $\text{\AA}^{-3}$ )	Barrier energy (eV)
$\text{Na}_3\text{FS}$	0.0003	0.47	0.44
$\text{Na}_3\text{FSe}$	0.0002	0.83	0.50
$\text{Na}_3\text{FTe}$	0.0001	0.94	0.55

Material [71]). A clear increase in Na diffusivity is revealed by the increase in the slope of the Na-MSD vs time at 700 K (Fig. 3). In Fig. 3(a), we compare the Na MSD at 700 K for all three compounds, while Fig. 3(b) shows the estimated diffusion constant ( $D$ ) from the MSD. We observe the largest diffusivity in  $\text{Na}_3\text{FS}$  followed by  $\text{Na}_3\text{FSe}$  and  $\text{Na}_3\text{FTe}$ . The estimated  $D$  at 700 K are, respectively,  $0.63 \times 10^{-6}$ ,  $0.19 \times 10^{-6}$ , and  $0.16 \times 10^{-6} \text{ cm}^2/\text{s}$  [Fig. 3(b)]. An earlier report on bulk ionic conductivity measurements on  $\text{Na}_{2.9}\text{FS}_{0.9}\text{I}_{0.1}$  shows [55] the change in conductivity by  $\sim 4$  times from 300 to 400 K, and extrapolation of experimental data at 700 K leads to  $\sim 14$  times enhancement in ionic conductivity, which is in fair agreement with the calculated change in the diffusion coefficient as estimated from the MSD (Fig. S3 in the Supplemental Material [71]) from 300 to 700 K for 2% Na-vacant  $\text{Na}_3\text{FS}$ .

To probe the possible pathways of Na diffusion, we have computed the Na probability density in the cubic phase with 2% Na vacancies at 700 K, as shown in Fig. 1. The probability density connects the nearest neighbor Na, which suggests the diffusion pathways. Interestingly, the probability density plots show better connectivity of Na-Na sites in  $\text{Na}_3\text{FS}$  followed by  $\text{Na}_3\text{FSe}$  and  $\text{Na}_3\text{FTe}$ , respectively, which is a clear manifestation of faster Na diffusion in  $\text{Na}_3\text{FS}$  than in the other two compounds. The barrier for Na hopping,  $E_B$  is calculated from the Na probability density using the following relation [77]:

$$E_B = -k_B T \ln \left( \frac{\rho_{\text{th}}}{\rho_{\text{max}}} \right).$$

Here,  $\rho_{\text{th}}$  and  $\rho_{\text{max}}$  are the threshold isosurface value at which the Na sites are just connected and the maximum isosurface value, and  $k_B$  is the Boltzmann constant (Table I). The estimated barrier energy for  $\text{Na}_3\text{FS}$  with 2% Na vacancy is  $\sim 0.44$  eV, which is in fair agreement with the reported total conductivity measurement with Na-vacant iodine-doped  $\text{Na}_3\text{FS}$  (0.44 eV) [55]. Similarly, for  $\text{Na}_3\text{FSe}$  and  $\text{Na}_3\text{FTe}$ , the barrier energy has been estimated (0.50 and 0.55 eV), as shown in Fig. 3(c).

To provide a visual understanding of Na-diffusion pathways, we draw the trajectory of one representative Na in  $\text{Na}_3\text{FS}$  in Fig. 4. A typical diffusion pathway, for example, from  $(\frac{1}{2} 0 0)$  to  $(0 \frac{1}{2} 0)$ , is as follows. Although the path follows a zigzag due to thermal vibrations, on average, the atom initially at  $(\frac{1}{2} 0 0)$  moves along the  $(0 1 0)$  direction as facilitated by the large vibrational amplitude of the soft phonons, then gradually redirects along the  $(-1 1 0)$  direction, and eventually moves along the  $(-1 0 0)$  direction to reach the next Na site. To investigate the correlations between Na hops in  $\text{FNa}_6$ , we have shown the MSD of all Na of a selected

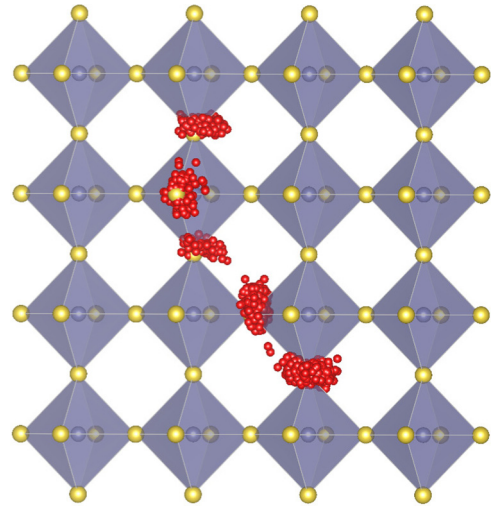


FIG. 4. The machine-learned molecular dynamics (MLMD) calculated time dependence of a representative Na ion (over 500 ps) in cubic  $\text{Na}_3\text{FS}$  structure with 2% vacancies at 700 K. The Na time-dependent trajectory (small red spheres) reveals the Na jumps to neighboring sites.

octahedron with one vacant site in Fig. S6 in the Supplemental Material [71] and observed that different Na hops are not correlated.

The computed Van Hove self-correlation function at 700 K with 2% Na vacancies  $G_s^{\text{Na}}(r, t)$  shows well-defined peaks corresponding to Na-Na jump distances (Fig. 5). We can observe the evolution of peaks in  $G_s^{\text{Na}}(r, t)$  with time at distances corresponding to Na intersite distances. It may be noted that the peak at  $\sim 3.2 \text{ \AA}$  in  $\text{Na}_3\text{FS}$  develops quicker than that in the other two compounds, consistent with the faster Na diffusion in  $\text{Na}_3\text{FS}$ . Additional time-averaged PDFs were computed between various atom pairs in 2% Na-vacant cubic- $\text{Na}_3\text{FY}$  ( $Y = \text{S, Se, Te}$ ) at 100, 300, and 700 K and are shown in Fig. S3 in the Supplemental Material [71].

Now, to investigate how the dynamics of host elements in cubic- $\text{Na}_3\text{FY}$  ( $Y = \text{S, Se, Te}$ ) with 2% Na vacancies influence the Na diffusion, we have performed constrained MLMD simulations with frozen  $Y$  and frozen host (i.e., both  $Y$  and  $F$ ) degrees of freedom. The calculated MSD from the constrained MLMD simulations is shown in Fig. 6. Strikingly, when we freeze the  $Y$ , or both  $Y$  and  $F$  sublattices, it strongly suppresses the Na-MSD, hence its diffusion. These indicate that the  $Y$  dynamics are essential for Na hopping. This may be understood as the displacement of  $Y$  atoms enabling the avoidance of the steric hindrance between the  $Y$  and the diffusing Na atoms.

#### IV. CONCLUSIONS

Through an extensive analysis of phonon SED and Van Hove correlation functions based on large-scale MLMD simulations, we have established the role of large anharmonicity of low- $E$  modes of wave vectors along the BZ edges in facilitating the diffusion process. These low- $E$  phonon modes involve large Na vibrations along the  $\langle 100 \rangle$  directions and are

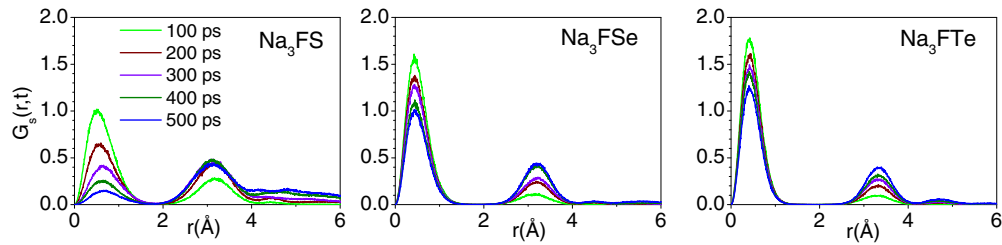


FIG. 5. The machine-learned molecular dynamics (MLMD) calculated self-Van Hove correlation function  $G_s(r, t)$  as a function of Na-Na distance ( $r$ ) at intervals of 100 ps in cubic  $\text{Na}_3\text{FY}$  ( $Y = \text{S}, \text{Se}, \text{Te}$ ) with 2% Na vacancies at 700 K. The evaluation of peak at 3.3 Å in  $G_s(r, t)$  indicates jumplike diffusion of the original atom (with  $r = 0$  at time  $t = 0$ ) to a neighboring site.

precursors for the Na hops in the crystal. Across the three compounds  $\text{Na}_3\text{FY}$  ( $Y = \text{S}, \text{Se}, \text{Te}$ ), the sulfide displays the softest (lowest energy) phonons along the BZ edges and the largest anharmonicity. These modes are rather floppy and overdamped. Due to the very large anharmonicity of these phonon modes, the net vibrations of neighboring Na atoms do not appear correlated. Further, the Na probability density calculation also shows the largest Na diffusion in  $\text{Na}_3\text{FS}$ , consistent with the experimental observations reported by Gao *et al.* [35].

We have thus shown that the anharmonicity of low- $E$  phonon modes in these antiperovskites is linked with Na diffusion. We have also revealed that the materials with lower Debye frequency or lower mean-phonon energy may not necessarily exhibit faster diffusion. Most importantly, we have

shown that host-element dynamics play an essential role in facilitating Na hops. Van Hove correlation function calculations identified that Na ions diffuse in a jumplike fashion. We have also established the need for defects, such as vacancies, to facilitate the diffusion in the crystalline lattice.

#### ACKNOWLEDGMENTS

The use of ANUPAM super-computing facility at Bhabha Atomic Research Centre is acknowledged. S.L.C. acknowledges the financial support of the Indian National Science Academy for the INSA Senior Scientist position. M.K.G. thanks Prof. Olivier Delaire for stimulating discussions and for his edits and comments.

M.K.G. and S.K. contributed equally to this paper.

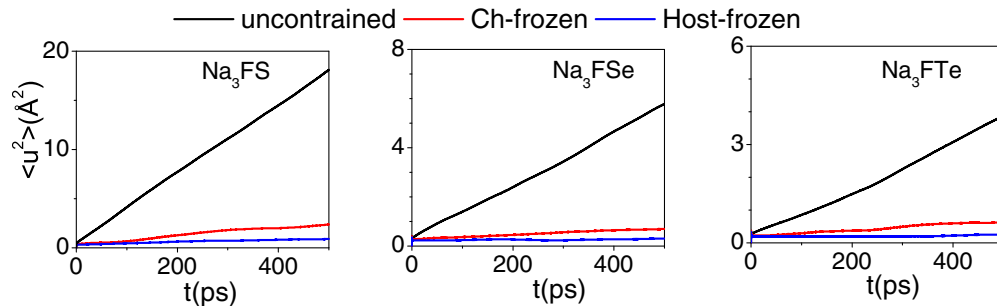


FIG. 6. The machine-learned molecular dynamics (MLMD) calculated Na-mean squared displacement (MSD) in cubic  $\text{Na}_3\text{FY}$  ( $Y = \text{S}, \text{Se}$  and  $\text{Te}$ ) with 2% Na vacancies at 700 K obtained from (i) unconstrained, (ii) with frozen-Ch, and (iii) with frozenhost (both Ch and F).

- [1] J. Janek and W. G. Zeier, *Nat. Energy* **1**, 016141 (2016).
- [2] A. J. E. Rettie, J. Ding, X. Zhou, M. J. Johnson, C. D. Malliakas, N. C. Osti, D. Y. Chung, R. Osborn, O. Delaire, S. Rosenkranz *et al.*, *Nat. Mater.* **20**, 1683 (2021).
- [3] A. Manthiram, X. Yu, and S. Wang, *Nat. Rev. Mater.* **2**, 016103 (2017).
- [4] J.-Y. Hwang, S.-T. Myung, and Y.-K. Sun, *Chem. Soc. Rev.* **46**, 3529 (2017).
- [5] Z. Zhang, Y. Shao, B. Lotsch, Y.-S. Hu, H. Li, J. Janek, L. F. Nazar, C.-W. Nan, J. Maier, M. Armand *et al.*, *Energy Environ. Sci.* **11**, 1945 (2018).
- [6] M. K. Gupta, J. Ding, D. Bansal, D. L. Abernathy, G. Ehlers, N. C. Osti, W. G. Zeier, and O. Delaire, *Adv. Energy Mater.* **12**, 2200596 (2022).
- [7] S. Chen, C. Wu, L. Shen, C. Zhu, Y. Huang, K. Xi, J. Maier, and Y. Yu, *Adv. Mater.* **29**, 1700431 (2017).
- [8] B. Singh, Z. Wang, S. Park, G. S. Gautam, J.-N. Chotard, L. Croguennec, D. Carlier, A. K. Cheetham, C. Masquelier, and P. Canepa, *J. Mater. Chem. A* **9**, 281 (2021).
- [9] M. Chen, W. Hua, J. Xiao, D. Cortie, W. Chen, E. Wang, Z. Hu, Q. Gu, X. Wang, S. Indris *et al.*, *Nat. Commun.* **10**, 001480 (2019).
- [10] J. S. Ko, P. P. Paul, G. Wan, N. Seitzman, R. H. DeBlock, B. S. Dunn, M. F. Toney, and J. Nelson Weker, *Chem. Mater.* **32**, 3028 (2020).
- [11] Z. Zou, N. Ma, A. Wang, Y. Ran, T. Song, B. He, A. Ye, P. Mi, L. Zhang, H. Zhou *et al.*, *Adv. Funct. Mater.* **31**, 2107747 (2021).

- [12] J. Zhang, Y. Liu, X. Zhao, L. He, H. Liu, Y. Song, S. Sun, Q. Li, X. Xing, and J. Chen, *Adv. Mater.* **32**, 1906348 (2020).
- [13] M. K. Gupta, J. Ding, N. C. Osti, D. L. Abernathy, W. Arnold, H. Wang, Z. Hood, and O. Delaire, *Energy Environ. Sci.* **14**, 6554 (2021).
- [14] S. Ohno, T. Bernges, J. Buchheim, M. Duchardt, A.-K. Hatz, M. A. Kraft, H. Kwak, A. L. Santhosha, Z. Liu, N. Minafra *et al.*, *ACS Energy Lett.* **5**, 910 (2020).
- [15] I. Hanghofer, B. Gadermaier, and H. M. R. Wilkening, *Chem. Mater.* **31**, 4591 (2019).
- [16] R. Schlem, P. Till, M. Weiss, T. Krauskopf, S. P. Culver, and W. G. Zeier, *Chem. Eur. J.* **25**, 4143 (2019).
- [17] M. Jansen and U. Henseler, *J. Solid State Chem.* **99**, 110 (1992).
- [18] X. Feng, H. Fang, P. Liu, N. Wu, E. C. Self, L. Yin, P. Wang, X. Li, P. Jena, and J. Nanda, *Angew. Chem. Int. Ed.* **60**, 26158 (2021).
- [19] M. A. Kraft, L. M. Gronych, T. Famprikis, and W. G. Zeier, *ACS Appl. Energy Mater.* **4**, 7250 (2021).
- [20] M. A. Kraft, L. M. Gronych, T. Famprikis, S. Ohno, and W. G. Zeier, *Chem. Mater.* **32**, 6566 (2020).
- [21] M. Duchardt, S. Neuberger, U. Ruschewitz, T. Krauskopf, W. G. Zeier, J. S. A. D. Günne, S. Adams, B. Roling, and S. Dehnen, *Chem. Mater.* **30**, 4134 (2018).
- [22] T. Krauskopf, S. Muy, S. P. Culver, S. Ohno, O. Delaire, Y. Shao-Horn, and W. G. Zeier, *J. Am. Chem. Soc.* **140**, 14464 (2018).
- [23] H. Gamo, N. H. H. Phuc, H. Muto, and A. Matsuda, *ACS Appl. Energy Mater.* **4**, 6125 (2021).
- [24] Q. Zhang, C. Zhang, Z. D. Hood, M. Chi, C. Liang, N. H. Jalarvo, M. Yu, and H. Wang, *Chem. Mater.* **32**, 2264 (2020).
- [25] R. Jalem, A. Hayashi, F. Tsuji, A. Sakuda, and Y. Tateyama, *Chem. Mater.* **32**, 8373 (2020).
- [26] S. Yubuchi, A. Ito, N. Masuzawa, A. Sakuda, A. Hayashi, and M. Tatsumisago, *J. Mater. Chem. A* **8**, 1947 (2020).
- [27] K. H. Park, D. H. Kim, H. Kwak, S. H. Jung, H.-J. Lee, A. Banerjee, J. H. Lee, and Y. S. Jung, *J. Mater. Chem. A* **6**, 17192 (2018).
- [28] H. Wang, *ACS Appl. Energy Mater.* **1**, 7028 (2018).
- [29] A. Banerjee, K. H. Park, J. W. Heo, Y. J. Nam, C. K. Moon, S. M. Oh, S.-T. Hong, and Y. S. Jung, *Angew. Chem. Int. Ed.* **55**, 9634 (2016).
- [30] M. K. Gupta, R. Mittal, B. Singh, O. Delaire, S. N. Achary, S. Rols, A. K. Tyagi, and S. L. Chaplot, *Phys. Rev. B* **103**, 174109 (2021).
- [31] M. K. Gupta, R. Mittal, S. Kumar, B. Singh, N. H. Jalarvo, O. Delaire, R. Shukla, S. N. Achary, A. I. Kolesnikov, A. K. Tyagi *et al.*, *J. Mater. Chem. A* **9**, 16129 (2021).
- [32] M. K. Gupta, B. Singh, P. Goel, R. Mittal, S. Rols, and S. L. Chaplot, *Phys. Rev. B* **99**, 224304 (2019).
- [33] R. Mittal, S. Kumar, M. K. Gupta, S. K. Mishra, S. Mukhopadhyay, M. Duc Le, R. Shukla, S. N. Achary, A. K. Tyagi, and S. L. Chaplot, *Mater. Adv.* **3**, 2104 (2022).
- [34] J. A. Dawson, T. Famprikis, and K. E. Johnston, *J. Mater. Chem. A* **9**, 18746 (2021).
- [35] S. Gao, T. Broux, S. Fujii, C. Tassel, K. Yamamoto, Y. Xiao, I. Oikawa, H. Takamura, H. Ubukata, Y. Watanabe *et al.*, *Nat. Commun.* **12**, 201 (2021).
- [36] L. Gao, H. Zhang, Y. Wang, S. Li, R. Zhao, Y. Wang, S. Gao, L. He, H.-F. Song, R. Zou *et al.*, *J. Mater. Chem. A* **8**, 21265 (2020).
- [37] Y. Sun, Y. Wang, X. Liang, Y. Xia, L. Peng, H. Jia, H. Li, L. Bai, J. Feng, and H. Jiang, *J. Am. Chem. Soc.* **141**, 5640 (2019).
- [38] Y. Zhao and L. L. Daemen, *J. Am. Chem. Soc.* **134**, 15042 (2012).
- [39] A. Emly, E. Kioupakis, and A. Van der Ven, *Chem. Mater.* **25**, 4663 (2013).
- [40] H. Fang and P. Jena, *Proc. Natl. Acad. Sci. USA* **114**, 11046 (2017).
- [41] R. Chen, Z. Xu, Y. Lin, B. Lv, S.-H. Bo, and H. Zhu, *ACS Appl. Energy Mater.* **4**, 2107 (2021).
- [42] X. Lü, G. Wu, J. W. Howard, A. Chen, Y. Zhao, L. L. Daemen, and Q. Jia, *Chem. Commun.* **50**, 11520 (2014).
- [43] M. K. Sugumar, T. Yamamoto, M. Motoyama, and Y. Iriyama, *Chem. Lett.* **50**, 448 (2021).
- [44] J. Zheng, B. Perry, and Y. Wu, *ACS Mater. Au* **1**, 92 (2021).
- [45] Y. Wang, Q. Wang, Z. Liu, Z. Zhou, S. Li, J. Zhu, R. Zou, Y. Wang, J. Lin, and Y. Zhao, *J. Power Sources* **293**, 735 (2015).
- [46] E. Ahiavi, J. A. Dawson, U. Kudu, M. Courty, M. S. Islam, O. Clemens, C. Masquelier, and T. Famprikis, *J. Power Sources* **471**, 228489 (2020).
- [47] J. Zheng, H. Fang, L. Fan, Y. Ren, P. Jena, and Y. Wu, *J. Phys. Chem. Lett.* **12**, 7120 (2021).
- [48] L. Yin, H. Yuan, L. Kong, Z. Lu, and Y. Zhao, *Chem. Commun.* **56**, 1251 (2020).
- [49] H. Fang, S. Wang, J. Liu, Q. Sun, and P. Jena, *J. Mater. Chem. A* **5**, 13373 (2017).
- [50] Z. Wang, H. Xu, M. Xuan, and G. Shao, *J. Mater. Chem. A* **6**, 73 (2018).
- [51] M.-H. Chen, A. Emly, and A. Van der Ven, *Phys. Rev. B* **91**, 214306 (2015).
- [52] A. C. Ferreira, S. Paofai, A. Létoublon, J. Ollivier, S. Raymond, B. Hehlen, B. Rufflé, S. Cordier, C. Katan, J. Even *et al.*, *Commun. Phys.* **3**, 48 (2020).
- [53] L. D. Whalley, J. M. Skelton, J. M. Frost, and A. Walsh, *Phys. Rev. B* **94**, 220301 (2016).
- [54] T. Lanigan-Atkins, X. He, M. J. Krogstad, D. M. Pajeroski, D. L. Abernathy, G. N. M. N. Xu, Z. Xu, D. Y. Chung, M. G. Kanatzidis, S. Rosenkranz *et al.*, *Nat. Mater.* **20**, 977 (2021).
- [55] S. Fujii, S. Gao, C. Tassel, T. Zhu, T. Broux, K. Okada, Y. Miyahara, A. Kuwabara, and H. Kageyama, *J. Am. Chem. Soc.* **143**, 10668 (2021).
- [56] C. Yu, S. Ganapathy, N. J. De Klerk, E. R. van Eck, and M. Wagemaker, *J. Mater. Chem. A* **4**, 15095 (2016).
- [57] L. Zhang, K. Yang, J. Mi, L. Lu, L. Zhao, L. Wang, Y. Li, and H. Zeng, *Adv. Energy Mater.* **5**, 1501294 (2015).
- [58] G. Kresse and J. Furthmüller, *Phys. Rev. B* **54**, 11169 (1996).
- [59] G. Kresse and J. Furthmüller, *Comput. Mater. Sci.* **6**, 15 (1996).
- [60] G. Kresse and D. Joubert, *Phys. Rev. B* **59**, 1758 (1999).
- [61] J. Perdew, K. Burke, and M. Ernzerhof, *Phys. Rev. Lett.* **80**, 891 (1998).
- [62] J. P. Perdew, K. Burke, and M. Ernzerhof, *Phys. Rev. Lett.* **77**, 3865 (1996).
- [63] A. Togo and I. Tanaka, *Scr. Mater.* **108**, 1 (2015).
- [64] H. J. Monkhorst and J. D. Pack, *Phys. Rev. B* **13**, 5188 (1976).
- [65] H. Wang, L. Zhang, J. Han, and W. E., *Comput. Phys. Commun.* **228**, 178 (2018).
- [66] S. Plimpton, *J. Comput. Phys.* **117**, 1 (1995).

- [67] H. Niu, L. Bonati, P. M. Piaggi, and M. Parrinello, *Nat. Commun.* **11**, 002654 (2020).
- [68] T. E. Gartner, L. Zhang, P. M. Piaggi, R. Car, A. Z. Panagiotopoulos, and P. G. Debenedetti, *Proc. Natl. Acad. Sci. USA* **117**, 26040 (2020).
- [69] R. Li, E. Lee, and T. Luo, *Mater. Today Phys.* **12**, 100181 (2020).
- [70] D. Lu, H. Wang, M. Chen, L. Lin, R. Car, E. W., W. Jia, and L. Zhang, *Comput. Phys. Commun.* **259**, 107624 (2021).
- [71] See Supplemental Material at <http://link.aps.org/supplemental/10.1103/PhysRevB.106.014311> for PDF, partial PDOS, and SED in Na-vacant systems of Na<sub>3</sub>FY ( $Y = S, Se, Te$ ). The AIMD and MLMD simulation details are also provided.
- [72] G. Kresse and J. Hafner, *Phys. Rev. B* **47**, 558(R) (1993).
- [73] L. Van Hove, *Phys. Rev.* **95**, 1374 (1954).
- [74] J.-P. Hansen and I. R. McDonald, *Theory of Simple Liquids: With Applications to Soft Matter* (Academic Press, Oxford, 2013).
- [75] J. A. Thomas, J. E. Turney, R. M. Iutzi, C. H. Amon, and A. J. McGaughey, *Phys. Rev. B* **81**, 081411 (2010).
- [76] D. Wendt, E. Bozin, J. Neuefeind, K. Page, W. Ku, L. Wang, B. Fultz, A. V. Tkachenko, and I. A. Zaliznyak, *Sci. Adv.* **5**, eaay2748 (2019).
- [77] K. Sau, T. Ikeshoji, S. Kim, S. Takagi, and S.-i. Orimo, *Chem. Mater.* **33**, 2357 (2021).